

# IRIS: Inverse Rendering of Indoor Scenes from Low Dynamic Range Images

Zhi-Hao Lin<sup>1,2</sup> Jia-Bin Huang<sup>1,3</sup> Zhengqin Li<sup>1</sup> Zhao Dong<sup>1</sup> Christian Richardt<sup>1</sup>  
 Tuotuo Li<sup>1</sup> Michael Zollhöfer<sup>1</sup> Johannes Kopf<sup>1</sup> Shenlong Wang<sup>2</sup> Changil Kim<sup>1</sup>

<sup>1</sup>Meta <sup>2</sup>University of Illinois Urbana-Champaign <sup>3</sup>University of Maryland College Park

<https://irisldr.github.io/>

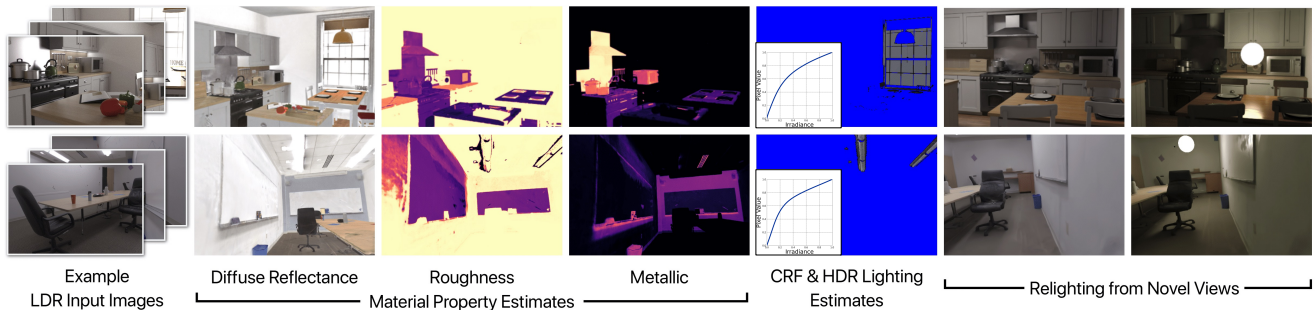


Figure 1. **Physically-based inverse rendering from LDR images.** Our method takes LDR input images and recovers high-quality spatially-varying HDR lighting, physically-based material properties, and a camera response function (CRF). The top row shows the result from a synthetic scene, and at the bottom, a real-world scene. The blue regions denote the non-emitting regions in the lighting maps. Reconstructed material allows us to relight the scene or insert new light sources or objects in a physically accurate manner.

## Abstract

While numerous 3D reconstruction and novel-view synthesis methods allow for photorealistic rendering of a scene from multi-view images easily captured with consumer cameras, they bake illumination in their representations and fall short of supporting advanced applications like material editing, relighting, and virtual object insertion. The reconstruction of physically based material properties and lighting via inverse rendering promises to enable such applications. However, most inverse rendering techniques require high dynamic range (HDR) images as input, a setting that is inaccessible to most users. We present a method that recovers the physically based material properties and spatially-varying HDR lighting of a scene from multi-view, low-dynamic-range (LDR) images. We model the LDR image formation process in our inverse rendering pipeline and propose a novel optimization strategy for material, lighting, and a camera response model. We evaluate our approach with synthetic and real scenes compared to the state-of-the-art inverse rendering methods that take either LDR or HDR input. Our method outperforms existing methods taking LDR images as input, and allows for highly realistic relighting and object insertion.

## 1. Introduction

Physically-based inverse rendering enables the reconstruction of realistic material properties and lighting information of a scene from multiple input images. Such a decomposition is useful for various applications, including relighting, material editing, and realistic object insertion. However, existing inverse rendering methods typically require input images to retain the high dynamic range (HDR) of the scene’s light transport. This poses a significant barrier to wide adoption and applicability, as HDR capture requires special hardware or merging multiple aligned LDR images via exposure bracketing [34].

Most common imaging sensors do not capture sufficient dynamic range for scenes’ light-emitting and non-emitting parts. Moreover, camera software often converts raw sensor readings to 8-bit low-dynamic-range (LDR) images for storage and transmission. The non-linear mapping and quantization lead to the additional loss of lighting information. The complex light transport in indoor environments makes it even more challenging to reconstruct the original HDR lighting, which is critical for faithful inverse rendering. Enabling material and lighting estimation from a “casual” capture, e.g., using your own camera or phone, would make inverse rendering much more accessible to users.

While many state-of-the-art inverse rendering methods

expect HDR inputs, some attempt to overcome this issue by taking LDR images as inputs and solving for the lighting with physically-based rendering. However, these methods often assume infinite far-away lighting [40], or require additional inputs, such as emitter masks [52]. While these assumptions may be acceptable for object-centric or outdoor scenes, these methods cannot handle the complex light transport of indoor scenes. Others use single-image input with a learned prior [25, 39], which cannot reconstruct high-quality full indoor scenes. On the other hand, multiple approaches [2, 38, 51] decompose radiance fields into materials and lighting from LDR input. However, most focus on *object-centric* scenes, and scene-level relighting and object insertion in those neural representations remain non-trivial.

We propose an inverse rendering method for indoor scenes with spatially varying illumination from multi-view LDR images with unknown varying exposures. Our method models tone mapping, i.e., the HDR-to-LDR conversion, so input LDR images can be consumed directly. We estimate spatially-varying HDR lighting via physically-based rendering (PBR), and optimize PBR material properties and the camera response function (CRF). Estimating all three jointly, however, leads to unstable optimization due to the ambiguities among lighting, albedo, and CRF. We design an optimization strategy that overcomes these ambiguities and enables high-quality estimation of all three. We compare our methods with several state-of-the-art inverse rendering methods, including those taking HDR input.

Our core contributions are:

- We propose a method to faithfully estimate spatially-varying HDR lighting and accurate physically-based materials from LDR input using physically-based rendering.
- We explicitly model LDR image formation in our (inverse) rendering pipeline, such that LDR images can be used directly, with either constant or varying exposure settings.
- Finally, we propose an optimization strategy to alternately optimize the spatially varying HDR lighting, PBR materials, and the camera response function.

## 2. Related Work

**Data-driven inverse rendering.** Numerous methods employ deep priors learned from large-scale datasets to tackle complex inverse rendering problems, including intrinsic image decomposition [20, 21], SVBRDF estimation [7, 19, 22, 53], lighting estimation [8, 23, 37], lighting editing [25] and relighting [33]. Those learning-based methods, often requiring only a single or a few images [2, 37] as inputs, significantly reduce capturing requirements of classical measurement-based methods [10]. High-quality datasets are essential for data-driven methods to achieve compelling generalization ability. Synthetic datasets are often used for training because ground-truth labeling is too challenging

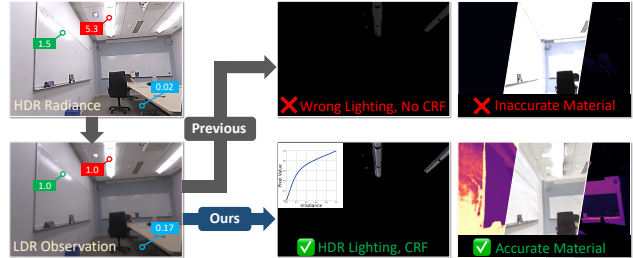


Figure 2. **Motivation.** A typical image formation process causes the loss of lighting information (e.g., emitter and reflection are both clipped to 1.0), posing a formidable challenge to most inverse rendering methods that require HDR input. Our proposed method not only recovers the HDR lighting and CRF, but also estimates accurate materials. We show normalized emission intensity.

to obtain in real environments. Despite efforts to create a photorealistic synthetic dataset [20, 24, 35], the inherent diversity of real-world environments, especially in complex indoor scenes, still causes a substantial domain gap. Our method uses predictions from a data-driven method [53] for initialization but achieves superior inverse rendering accuracy through a carefully designed optimization process.

**Optimization-based inverse rendering.** Inverse rendering seeks to reconstruct a scene’s geometry, material, and lighting from single or multiple images. This process is notoriously challenging and ill-posed due to the inherent ambiguity among these high-dimensional scene components. As differentiable path tracing (DPT) [14] enables optimization of scene parameters with physically-based multi-bounce light transport, recent methods exploit it to achieve high-quality disentanglement for scene factorization. Both IPT [1] and MILO [45] utilize DPT to jointly optimize dense-scene BRDF and lighting emission, accounting for global light transport. IPT and the follow-up work [32] take a piecewise constant parameterization of material to reduce Monte-Carlo variance and ambiguity, losing fine spatial details as a result. MILO supports complex material representation while exhibiting very slow convergence. Besides the subpar material reconstruction quality, these methods all require HDR images as input, limiting their practical applications. The recent factorized inverse path tracing (FIPT) method [42] utilizes a factored light transport formulation and finds emitters driven by rendering errors, thus achieving high-quality reconstruction of spatially-varying lighting and surface materials. However, FIPT is designed to take HDR images as input for best performance. To practically and faithfully estimate spatially varying HDR lighting and materials with solely LDR images, we built a novel inverse rendering pipeline upon FIPT [42] while explicitly modeling LDR image formation and introducing a novel alternating optimization strategy.

Recent NeRF-based approaches like I<sup>2</sup>-SDF [52], NeILF++ [49], and NeFII [41], much like FIPT, rely on pre-calculated irradiance and focus on surface rendering to recon-

struct scene materials and lighting. However, these methods typically account for only single-bounce light transport, compromising material and lighting reconstruction quality.

**CRF and HDR estimation.** The complete information about the illumination is usually lost within the photography pipeline, where the original radiance is clipped, converted with CRF, and then quantized to a common image format. Estimating the HDR lighting and camera CRF enables us to edit photos and achieve realistic object insertion. Debevec and Malik [6] propose to take multiple photos with varying exposure levels and formulate an optimization to recover the CRF and HDR image with SVD. Grossberg and Nayar [11] collected and analyzed the CRF from real-world devices and proposed an empirical model of response (EMoR) as a low-dimensional CRF parameterization, enabling estimation from sparser input. Some previous works [27, 29, 43, 47] predict HDR images with a data-driven approach by learning LDR–HDR mapping from a single image. However, these methods rely on HDR data for training, and the estimation is inconsistent across views and scenes.

Another line of research targets estimating lighting parameters for realistic object insertion. Some work [5, 9, 12, 13, 48] predict HDR environment maps from single images for outdoor and indoor scenes. However, the environment map does not represent the indoor illumination well. Wang et al. Wang et al. [39] and FEGR [40] leverage physically-based rendering and optimize HDR lighting from single/multiple images but do not address inverse rendering for indoor scenes. We leverage physically-based rendering and multi-view cues to recover spatially varying BRDF, HDR illumination, and CRF from LDR images. Our method generates realistic view synthesis, relighting, and object insertion with accurate decomposition.

### 3. Background: Factorized Light Transport

We start by briefly summarizing the adopted light transport model. We follow the rendering equation [16] to model physically-based light transport for realistic rendering:

$$\mathbf{L}_o(\mathbf{x}, \boldsymbol{\omega}_o) = \mathbf{L}_e(\mathbf{x}, \boldsymbol{\omega}_o) + \int_{\Omega^+} \mathbf{L}_i(\mathbf{x}, \boldsymbol{\omega}_i) f(\mathbf{x}, \boldsymbol{\omega}_i, \boldsymbol{\omega}_o) d\boldsymbol{\omega}_i, \quad (1)$$

where  $\mathbf{L}_o$  is the radiance observed along a ray  $(\mathbf{x}, \boldsymbol{\omega}_o)$  for a 3D position  $\mathbf{x}$  and a direction  $\boldsymbol{\omega}_o$ ,  $\mathbf{L}_e$  is the emission term,  $\mathbf{L}_r = \int_{\Omega^+} \mathbf{L}_i(\mathbf{x}, \boldsymbol{\omega}_i) f(\mathbf{x}, \boldsymbol{\omega}_i, \boldsymbol{\omega}_o) d\boldsymbol{\omega}_i$  is the reflectance term, and  $f(\mathbf{x}, \boldsymbol{\omega}_i, \boldsymbol{\omega}_o)$  is the BRDF. While  $\mathbf{L}_i$  encapsulates recursive incident radiance computation, we represent spatially-varying materials using the Cook-Torrance BRDF [4]:

$$f(\mathbf{x}, \boldsymbol{\omega}_i, \boldsymbol{\omega}_o) = \frac{\mathbf{k}_d(\mathbf{x})}{\pi} (\mathbf{n} \cdot \boldsymbol{\omega}_i)_+ + \frac{F \cdot D \cdot G}{4(\mathbf{n} \cdot \boldsymbol{\omega}_o)}, \quad (2)$$

where  $D(\mathbf{h}, \mathbf{n}, \sigma(\mathbf{x}))$  describes the distribution of microfacet orientations,  $G(\boldsymbol{\omega}_i, \boldsymbol{\omega}_o, \mathbf{n}, \sigma(\mathbf{x}))$  encodes the masking and

shadowing effects between microfacets, and  $F(\boldsymbol{\omega}_i, \mathbf{h}, \mathbf{k}_s(\mathbf{x}))$  is a Fresnel reflection term. The recursive integral in Equation 1 is computationally expensive and usually approximated with Monte-Carlo path tracing [16, 18] with multiple bounces. The rendering equation can be accelerated by factorizing the BRDF term from the integral [17, 36, 39]:

$$\mathbf{L}_r(\mathbf{x}, \boldsymbol{\omega}_o) = \mathbf{k}_d \mathbf{L}_d(\mathbf{x}) + \mathbf{k}_s \mathbf{L}_s^0(\mathbf{x}, \boldsymbol{\omega}_o, \sigma) + \mathbf{L}_s^1(\mathbf{x}, \boldsymbol{\omega}_o, \sigma), \quad (3)$$

where we decompose the reflectance term into a diffuse shading term  $\mathbf{L}_d(\mathbf{x}) = \int_{\Omega^+} \mathbf{L}_i(\mathbf{x}, \boldsymbol{\omega}_i) \frac{(\mathbf{n} \cdot \boldsymbol{\omega}_i)_+}{\pi} d\boldsymbol{\omega}_i$ , as well as two specular terms  $\mathbf{L}_s^0(\mathbf{x}, \boldsymbol{\omega}_o, \sigma) = \int_{\Omega^+} \mathbf{L}_i(\mathbf{x}, \boldsymbol{\omega}_i) \frac{F_0 D G}{4(\mathbf{n} \cdot \boldsymbol{\omega}_o)} d\boldsymbol{\omega}_i$  and  $\mathbf{L}_s^1(\mathbf{x}, \boldsymbol{\omega}_o, \sigma) = \int_{\Omega^+} \mathbf{L}_i(\mathbf{x}, \boldsymbol{\omega}_i) \frac{F_1 D G}{4(\mathbf{n} \cdot \boldsymbol{\omega}_o)} d\boldsymbol{\omega}_i$ , where  $F_0 = 1 - F_1$  and  $F_1 = (1 - \mathbf{h} \cdot \boldsymbol{\omega}_i)^5$ .  $\mathbf{k}_d(\mathbf{x})$  is diffuse reflectance and  $\mathbf{k}_s(\mathbf{x})$  is specular reflectance calculated from the BRDF. The roughness  $\sigma$  is further factorized by linearly interpolating the shading maps baked at various roughness levels:  $\mathbf{L}_s^*(\cdot, \sigma) = \text{LERP}(\{\mathbf{L}_s^*(\cdot, \sigma_i)\}_{i=1}^6, \sigma)$ , where  $\{\sigma_i\}_{i=1}^6$  is uniformly sampled between  $(0, 1)$ . With the factorization formulation, the shading maps  $\mathbf{L}_d$ ,  $\{\mathbf{L}_s^0(\cdot, \sigma_i), \mathbf{L}_s^1(\cdot, \sigma_i)\}_{i=1}^6$  can be pre-baked and allow for more efficient and stable optimization of material properties and HDR lighting.

**Tone Mapping.** Rendering is typically performed in HDR, requiring a comprehensive image formation process to produce the final LDR image for display. Tone mapping is crucial as it maps HDR content to LDR, often using a nonlinear camera response function (CRF). Specifically, to produce LDR images, we apply the CRF to the calculated HDR radiance with the exposure level  $t_i$ :

$$\hat{\mathbf{I}}_i = \text{CRF}(\mathbf{L}_o(\mathbf{x}, \boldsymbol{\omega}_o); t_i). \quad (4)$$

## 4. Representation

**Material BRDF.** The surface albedo  $\mathbf{a}(\mathbf{x}) \in \mathbb{R}^3$ , roughness  $\sigma(\mathbf{x}) \in \mathbb{R}$ , and metallic  $m(\mathbf{x}) \in \mathbb{R}$  model the diffuse reflectance  $\mathbf{k}_d = \mathbf{a} \cdot (1 - m)$  and specular reflectance  $\mathbf{k}_s = 0.04 \cdot (1 - m)$ , and are parameterized as a neural field  $\mathbf{f}: \mathbf{x} \mapsto (\mathbf{a}, \sigma, m)$ .

**Camera response function (CRF).** The CRF is crucial for inverse rendering from 8-bit LDR images, as it allows recovery of the original radiance only when its inverse is known. However, the CRF varies with each camera and is often unknown to users. Therefore, deducing the CRF from LDR image observations is critical to our solution. The forward and inverse processes of the CRF could be expressed as:

$$\mathbf{c}_{\text{LDR}} = \text{CRF}(\mathbf{c}_{\text{HDR}}; t) = \mathbf{g}(\text{CLAMP}(t \cdot \mathbf{c}_{\text{HDR}}, 0, 1)), \quad (5)$$

$$\mathbf{c}'_{\text{HDR}} = \text{CRF}^{-1}(\mathbf{c}_{\text{LDR}}; t) = \frac{1}{t} \mathbf{g}^{-1}(\mathbf{c}_{\text{LDR}}), \quad (6)$$

where  $\mathbf{c}$  is an RGB color, and  $\mathbf{g}$  a generic (multi-channel) monotonic function. Note that  $\text{CRF}^{-1}$  and  $\text{CRF}$  are often not perfectly bijective due to the clamp and quantization error.

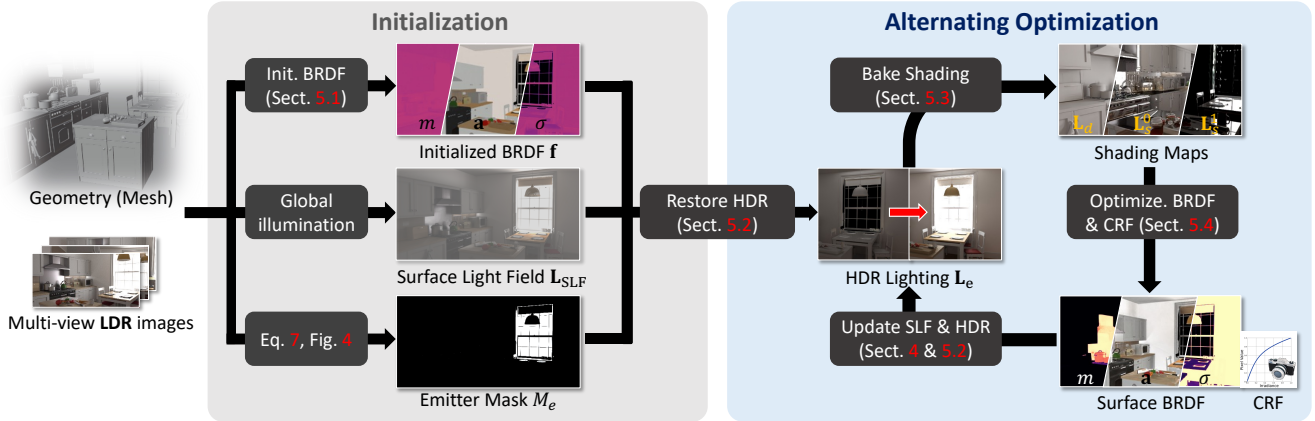


Figure 3. **Framework Overview.** Given multi-view posed LDR images and a surface mesh, our inverse rendering pipeline is divided into two main stages. In the initialization stage, we initialize the BRDF (Section 5.1), extract a surface light field (Section 4), and estimate emitter geometry (Equation 7). In the optimization stage, we first recover HDR radiance from the LDR input (Section 5.2), then bake shading maps (Section 5.3), and jointly optimize BRDF and CRF parameters (Section 5.4). The improved parameters are used to refine the emission again. These three steps are repeated until convergence.

In practice, we use Grossberg and Nayar’s empirical model of response (EMoR) for  $\mathbf{g}$  [27]. A mean curve  $\bar{\mathbf{g}}$  and PCA basis  $\mathbf{B}$  are collected and calculated from real-world devices, and the CRF is parameterized as  $\mathbf{g} = \bar{\mathbf{g}} + \mathbf{B}\mathbf{w}$ , where  $\mathbf{w}$  weighs each basis and controls the shape of the CRF. We discretize the function as  $\mathbf{g}(x) = \text{LERP}(\{g_k\}_k, x)$ , which linearly interpolates the uniformly sampled CRF  $\{g_k\}_{k=0}^{1023} \in [0, 1]^{1024}$ , independently per color channel.

**Spatially-varying lighting.** While environment maps handle object-centric and outdoor scenes well [15, 38, 40, 50], they cannot capture complex spatially-varying lighting of indoor scenes. To handle it, following FIPT [42], we define direct lighting on the surface mesh of the input scene and measure emission as view-independent radiance:  $\mathbf{L}_e(\mathbf{x}, \omega_o) = \mathbf{L}_e(\mathbf{x}) \in \mathbb{R}^3$ . We also define an emitter mask  $M_e(\mathbf{x}) \in \{0, 1\}$  to denote whether a surface point  $\mathbf{x}$  is on an emitter. Global illumination is represented as a view-independent surface light field (SLF):  $\mathbf{L}_{\text{SLF}}(\mathbf{x}) \in \mathbb{R}^3$ . The sRGB pixel colors of input LDR images are linearized with an inverse CRF:  $\mathbf{I}_{\text{linear}} = \text{CRF}^{-1}(\mathbf{I}_{\text{LDR}}; t_i)$ . If a voxel contains no surface, it is set to zero; otherwise, it collects the average linearized radiances across all input images with ray casting. This greatly accelerates the approximation of global illumination without requiring multi-bounce ray tracing.

## 5. Inverse Rendering from LDR Images

Given multi-view posed LDR images  $\{\mathbf{I}_i\}$  captured with the same or varying exposure levels  $\{t_i\}$ , our goal is to estimate spatially-varying HDR lighting, surface material (as albedo, roughness, and metallic), and the camera response function (CRF), shared by all input images. We assume the geometry is given, which can be efficiently and accurately estimated with off-the-shelf methods [26, 46, 52] for indoor scenes. We

further assume that the primary light sources are observed in the input images, following the recent literature [42, 45, 52].

Previous work [1, 32] performs differentiable path tracing during the material and lighting optimization, but the number of samples is limited due to heavy computation. This introduces high variance and unstable estimation. The factorized formulation (Section 3) of FIPT [42] splits light transport into BRDF parameters and shading and enables the update of them alternately. While the method is shown to be more stable and produce high-quality decompositions, it requires HDR images as input to aggregate and bake shading maps, detect emitters, and estimate HDR emissions.

To address this ill-posed optimization problem, we propose a multi-stage optimization strategy alternately estimating spatially varying lighting, material, and CRF. Specifically, we (1) initialize the BRDF with an off-the-shelf intrinsic decomposition method (Section 5.1), (2) recover HDR lighting from LDR with physically-based rendering (Section 5.2), (3) bake the diffuse and specular shading (Section 5.3), and (4) jointly estimate BRDF and CRF (Section 5.4). We repeat Steps 2–4 in that order until all estimates are converged. Figure 3 illustrates our framework.

### 5.1. BRDF Initialization

For each input image  $\mathbf{I}_i$ , we predict a 2D albedo map  $\mathbf{A}_i$  using an off-the-shelf single-image intrinsic decomposition method and averaging per-pixel albedo values within each semantic part. Given  $\{\mathbf{A}_i\}$ , we initialize albedo  $\mathbf{a}(\mathbf{x})$  by minimizing the error between the projected albedo and the estimated albedo across all input images:  $\min_{\mathbf{a}} \sum_i \|\pi_i(\mathbf{a}) - \mathbf{A}_i\|_2$ . Here,  $\pi_i$  represents the perspective projection onto the image space of  $\mathbf{I}_i$  by intersecting camera rays with the surface mesh of the input scene and reading  $\mathbf{a}$  at their first intersections. We use IrisFormer [53] for single-image albedo

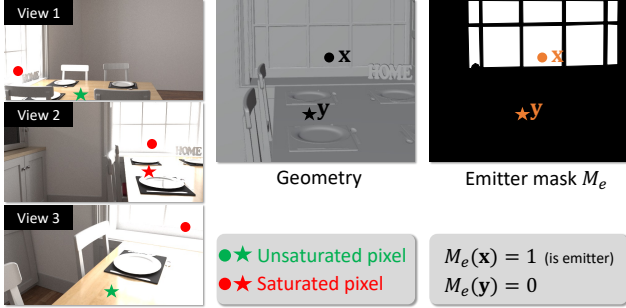


Figure 4. **Emitter mask estimation**  $M_e(\mathbf{x})$ . The projected point  $\mathbf{x}$  on the window is saturated across all input views and thus identified as an emitter. The point  $\mathbf{y}$  on the table is reflective and saturated in some views (e.g. view 2), but not in others, and is thus excluded in the emitter mask.

estimation, and obtain semantic category labels from part IDs in synthetic scenes or using Mask2Former [3] for real scenes. Roughness and metallic are both initialized to 0.5.

## 5.2. HDR Emission Restoration

Given that emitters appear bright across views and produce saturated pixels in LDR images, we estimate the binary emitter geometry  $M_e(\mathbf{x})$  on the surface mesh as follows:

$$M_e(\mathbf{x}) = \begin{cases} 1 & \text{if } \frac{1}{N} \sum_i v_i(\mathbf{x}) \mathbf{I}_i(\pi_i(\mathbf{x})) \geq 0.99 \\ 0 & \text{otherwise,} \end{cases} \quad (7)$$

where  $v(\cdot) \in \{0, 1\}$  indicates visibility. See Figure 4.

We perform physically-based rendering with single-bounce path tracing to generate the images (1). To estimate the radiance at the point  $\mathbf{x}$  observed from a camera ray, we trace  $N = 128$  secondary rays from  $\mathbf{x}$ , sampled with the current BRDF estimates. The resulting radiance is approximately estimated by:

$$\mathbf{L}_r(\mathbf{x}, \omega_o) = \sum_{i=1}^N \mathbf{L}_{\text{end}}(\mathbf{x}') f(\mathbf{x}, \omega_i, \omega_o), \quad (8)$$

$$\mathbf{L}_{\text{end}}(\mathbf{x}) = \begin{cases} \mathbf{L}_e(\mathbf{x}) & \text{if } M_e(\mathbf{x}) = 1 \\ \mathbf{L}_{\text{SLF}}(\mathbf{x}) & \text{otherwise,} \end{cases} \quad (9)$$

where  $\mathbf{x}' = \mathbf{x} + d \cdot \omega_i$  is the intersected point of the secondary ray along direction  $\omega_i$ . Intuitively, we retrieve the radiance from the *learnable* emission radiance  $\mathbf{L}_e(\mathbf{x})$  if the secondary ray hits an emitter directly, or otherwise from the pre-computed surface light field  $\mathbf{L}_{\text{SLF}}(\mathbf{x})$  to approximate the global illumination. Figure 5 shows an illustration.

To recover the HDR emitter radiance, we minimize the photometric loss with gradient descent:  $\min_{\mathbf{L}_e} \mathcal{L}_{\text{photo}}$ , where

$$\mathcal{L}_{\text{photo}} = \sum_i \|\text{CRF}(\mathbf{L}_o(\mathbf{x}, \omega_o); t_i) - \mathbf{I}_i\|_2. \quad (10)$$

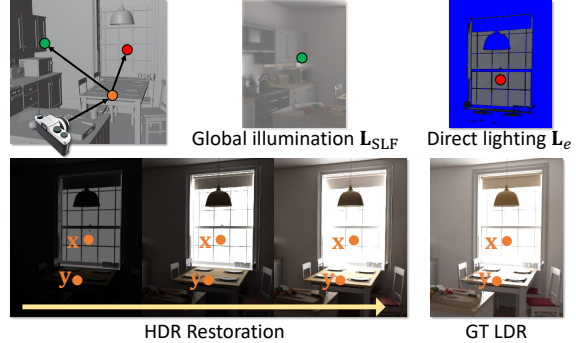


Figure 5. **HDR emission restoration**. **Top:** Ray sampling process. Learnable direct lighting  $\mathbf{L}_e$  is retrieved if a ray hits an emitter (e.g., window) or global illumination  $\mathbf{L}_{\text{SLF}}$  is retrieved otherwise (e.g., wall). **Bottom:** HDR restoration process. By performing differentiable physically-based rendering, the photometric loss at non-saturated pixel  $\mathbf{y}$  enhances the emitter intensity  $\mathbf{L}_e$ .

The emitter radiance  $\mathbf{L}_e(\mathbf{x})$  is enhanced to match the captured images, while the BRDF and CRF are fixed in this stage. The parameterization of  $\mathbf{L}_e(\mathbf{x})$  is detailed in our supplementary material.

## 5.3. Shading Baking

After the HDR emission is recovered in the previous stage, we bake the diffuse and specular shading maps  $\mathbf{L}_d$ ,  $\mathbf{L}_s^0$ ,  $\mathbf{L}_s^1$ , following factorized light transport (Section 3). Given a surface point intersected by a camera ray, multiple rays are sampled according to the current (fixed) BRDF. The incident radiance is computed with multi-bounce path tracing, following FIPT [42], where a ray keeps tracing if it hits a non-emissive specular surface and stops otherwise. The radiance of the endpoint follows Equation 9.

## 5.4. BRDF & CRF Optimization

With the baked shading maps  $\mathbf{L}_d$ ,  $\mathbf{L}_s^0$ , and  $\mathbf{L}_s^1$ , the albedo, metallic, roughness, and CRF are jointly optimized. The optimization involves the following objective function:

$$\min_{\mathbf{a}, m, \sigma, g} \mathcal{L}_{\text{photo}} + \lambda_a \mathcal{L}_{\text{albedo}} + \lambda_c \mathcal{L}_{\text{CRF}} + \lambda_m \mathcal{L}_{\text{mat}}, \quad (11)$$

where  $\lambda_a = 0.01$ ,  $\lambda_c = 0.001$ , and  $\lambda_m = 0.005$ .

**Photometric loss.** We perform physically-based rendering, and the photometric loss  $\mathcal{L}_{\text{photo}}$  is computed as in Eq. 10.

**Albedo regularization.** Motivated by the shift-scale-invariant loss in MonoSDF [46], we adopt a shift-invariant loss against the monocular albedo maps  $\{\mathbf{A}_i\}$ :

$$\mathcal{L}_{\text{albedo}} = \sum_i \|\pi_i(\mathbf{a}) - s \mathbf{A}_i\|_2, \quad (12)$$

where  $s$  is the scale used to align the two albedo maps.

**CRF regularization.** We regularize the  $L_2$  norm of the estimated coefficients of the PCA bases and enforce the

Table 1. **BRDF-emission comparison on synthetic data.** FIPT-LDR\* is provided with the GT emitter mask as additional input. The best metrics among LDR methods are highlighted in bold.

	Method	$k_d$	$a'$ PSNR $\uparrow$	$\sigma$	$I_c$	
					IoU $\uparrow$	L2 $\downarrow$
Kitchen	Li et al. [25]	15.75	12.64	10.15	0.43	1.410
	NeILF [44]	16.63	13.73	14.77	—	—
	FIPT-LDR*	15.77	8.97	5.94	<b>0.58</b>	0.450
	Ours	<b>23.22</b>	<b>17.52</b>	<b>20.35</b>	<b>0.58</b>	<b>0.203</b>
	FIPT-HDR [42]	34.34	27.05	24.55	0.88	0.010
Bedroom	Li et al. [25]	18.90	15.10	11.38	0.34	2.784
	NeILF [44]	16.85	13.99	16.03	—	—
	FIPT-LDR*	18.38	9.60	5.82	<b>0.77</b>	0.245
	Ours	<b>26.44</b>	<b>20.95</b>	<b>26.47</b>	<b>0.77</b>	<b>0.043</b>
	FIPT-HDR [42]	28.98	25.86	23.53	0.92	0.004
Livingroom	Li et al. [25]	16.78	14.71	11.42	0.17	3.610
	NeILF [44]	16.06	13.86	15.95	—	—
	FIPT-LDR*	11.59	8.93	4.08	<b>0.77</b>	0.240
	Ours	<b>18.09</b>	<b>15.45</b>	<b>25.28</b>	<b>0.77</b>	<b>0.103</b>
	FIPT-HDR [42]	28.42	27.47	30.44	0.95	0.005
Bathroom	Li et al. [25]	15.50	13.60	12.24	0.45	1.351
	NeILF [44]	17.85	14.49	<b>21.09</b>	—	—
	FIPT-LDR*	16.21	11.46	4.12	<b>0.62</b>	0.187
	Ours	<b>21.56</b>	<b>17.74</b>	13.43	<b>0.62</b>	<b>0.135</b>
	FIPT-HDR [42]	28.06	23.54	26.97	0.68	0.080

monotonicity of the sampled CRF as follows:

$$\mathcal{L}_{\text{CRF}} = \|\mathbf{w}\|_2 + \sum_i \max(g_{i-1} - g_i, 0). \quad (13)$$

**Material regularization.** We apply FIPT’s roughness-metallic regularization [42]. While the shading and emission are initially inaccurate and lead to erroneous BRDFs, we alternately update the BRDFs and produce better emission and shading, improving the BRDFs. Our alternating strategy yields more stable optimization and better estimation.

## 6. Experiments

We evaluate our method on both synthetic and real-world data in comparison to several baseline methods. We analyze the quality of our intrinsic decomposition, relighting, and novel-view synthesis capability. Please see our supplementary material for additional results and evaluations. We will release our code and data upon acceptance.

**Datasets.** We evaluate our method and all baselines on the FIPT dataset [42], which consists of four synthetic scenes and two real-world scenes. The synthetic scenes provide ground-truth geometry and material properties. For the real-world captures, we reconstruct the surface meshes using MonoSDF [46], which recovers the scene geometry as a neural signed distance field (SDF). We extract the final mesh with marching cubes [28]. We used the LDR images provided in the dataset, where the linear intensity is clipped

Table 2. **Quantitative results of novel view synthesis (NVS) and relighting on synthetic scenes.**

	Method	PSNR $\uparrow$	SSIM $\uparrow$	LPIPS $\downarrow$
NVS	NeILF [44]	<b>30.031</b>	0.899	<b>0.180</b>
	FIPT-LDR*	15.180	0.744	0.437
	Ours	29.468	<b>0.903</b>	0.181
	FIPT-HDR [42]	28.760	0.902	0.186
Relighting	Li22 [25]	22.444	0.813	0.398
	FIPT-LDR*	11.626	0.705	0.359
	Ours	<b>22.861</b>	<b>0.882</b>	<b>0.173</b>
	FIPT-HDR [42]	29.012	0.902	0.139

in bright regions, compressed with a nonlinear CRF, quantized into 256 levels, and stored in 8-bit PNG format. We adopt the constant exposure setting to provide a fair comparison with baselines since their methods cannot handle varying exposure. We further evaluate varying exposure settings in Section 6.5.

**Baselines.** We compare our method with these baselines. Li et al. [25] estimate BRDF, geometry (depth & normal), and lighting condition of an indoor scene from a single image using a data-driven approach. In addition to the single image, the model also takes emitter masks as input, and we provide the mask estimated by our method (7). NeILF [44] targets inverse rendering from known geometry and multi-view images. The spatially-varying BRDF and illumination are parameterized as neural fields [30]. Physically-based rendering and ray tracing are performed during the training and rendering process. The HDR-to-LDR tone mapping is modeled as learnable gamma correction. The original FIPT [42] is designed for HDR input, so the emission mask estimation cannot apply to LDR input. Thus, we additionally provide the method with the emission mask estimated by our method (7). We denote this modified version as ‘FIPT-LDR\*’.

To further evaluate our performance, we compare to the original FIPT with HDR input, denoted as ‘FIPT-HDR’. This privileged information will make illumination estimation much more accurate.

### 6.1. Intrinsic Decomposition on Synthetic Scenes

We compute the metrics of intrinsic decomposition and provide the comparison in Table 1. We follow the evaluation in FIPT [42] and compare the roughness  $\sigma$ , diffuse reflectance  $k_d$  among the diffuse surfaces, and material reflectance:  $a' = \int_{\Omega^+} f d\omega_i$  estimated with Monte Carlo integration. We report the PSNR for these BRDF estimates. For emission, we calculate the intersection over union (IoU) of the emission masks and compare the  $L_2$  error of estimated emission maps. All the estimates are rendered in image space and compared with ground truth.

Table 1 shows that our method surpasses all baseline methods that use LDR inputs regarding intrinsic decomposition quality. Compared to the state-of-the-art single-view

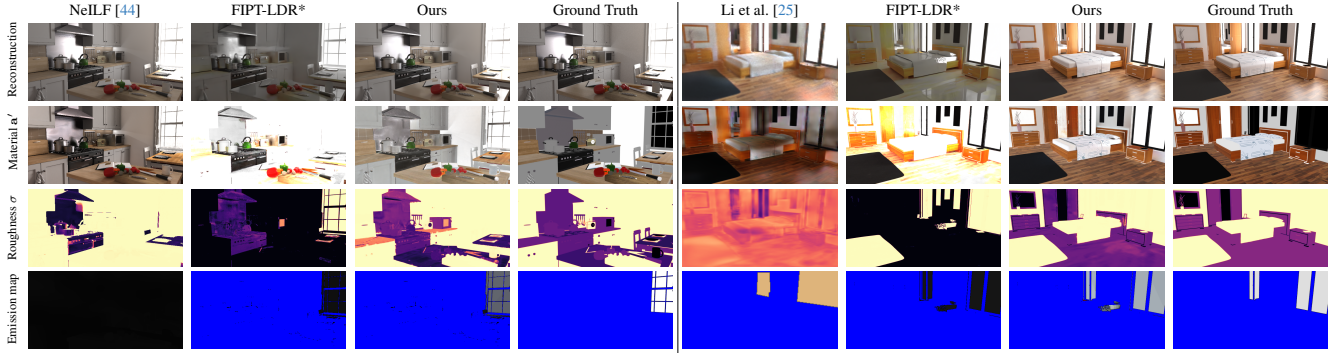


Figure 6. **Intrinsic decomposition of synthetic scenes [42]**. From top to bottom, we show reconstruction, material reflectance  $a'$ , roughness  $\sigma$ , and emitter map. Roughness is visualized with a false-color encoding (the warmer, the higher). For the emission map, we mask the non-emitter region in blue, and show normalized HDR emission otherwise, such that it is not saturated and differences become visible.

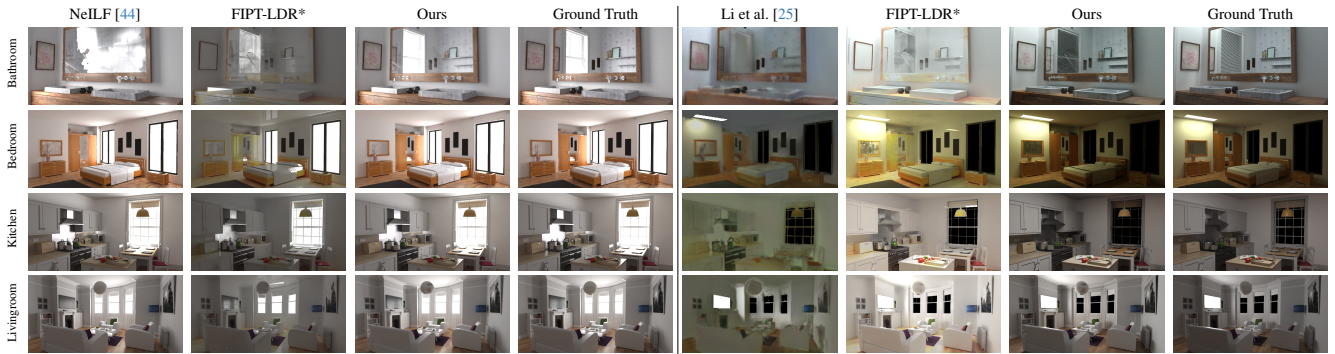


Figure 7. **Novel-view synthesis and relighting results on synthetic scenes [42]**. The novel view synthesis results are shown in the left four columns, and the relighting of the same novel view are shown in the right four columns.

method by Li et al. [25], our method excels in all metrics across various scenes, indicating superior decomposition of intrinsic properties from multi-view observations. Furthermore, even when the estimated emitter mask is provided for FIPT-LDR\*, it fails to recover emission radiance, leading to compromised BRDF estimation accurately. The  $L_2$  error of emission maps shows that our proposed HDR restoration (Section 5.2) successfully recovers the HDR lighting from LDR observations, which leads to better light transport modeling and more accurate BRDF estimation. FIPT-HDR takes HDR images as input and shows the best quality overall.

Figure 6 shows intrinsic decomposition, including image reconstruction, material reflectance  $a'$ , roughness  $\sigma$ , and emission maps. While NeILF [44] achieves accurate rendering, it bakes significant shading effects into its diffuse albedo map. Li et al. [25] generate a noisy BRDF from a single image input. FIPT-LDR\* tends to underestimate illumination intensity, overestimating the reflectance  $a'$  as compensation. In contrast, our method successfully recovers high-quality HDR emission from LDR input, resulting in precise intrinsic decomposition.

## 6.2. View Synthesis and Relighting

We compare novel view synthesis and relighting of all competing algorithms and report results in Table 2. Our method achieves competitive quality in novel view synthesis, on par with NeILF. The true strength of our method becomes apparent in relighting. Thanks to accurate BRDF modeling, our approach surpasses other LDR baselines.

The qualitative results are illustrated in Figure 7. While NeILF [44] cannot model mirror reflection with its light field representation, our method generates realistic results for such highly specular material. This shows that our method approximates the light transport with new illumination well and renders images closer to the ground truth.

## 6.3. Intrinsic Decomposition on Real Scenes

Besides synthetic scenes, we also evaluate two real scenes and show the intrinsic decomposition results in Figure 8. The comparison of the material reflectance field  $a'$  reveals that Li et al. [25] and FIPT-LDR\* struggle to remove strong shading and shadows. Still, our method recovers an almost shading-free albedo field. Regarding roughness, our method effectively identifies specular surfaces with low roughness values on the whiteboard in the right image, demonstrating

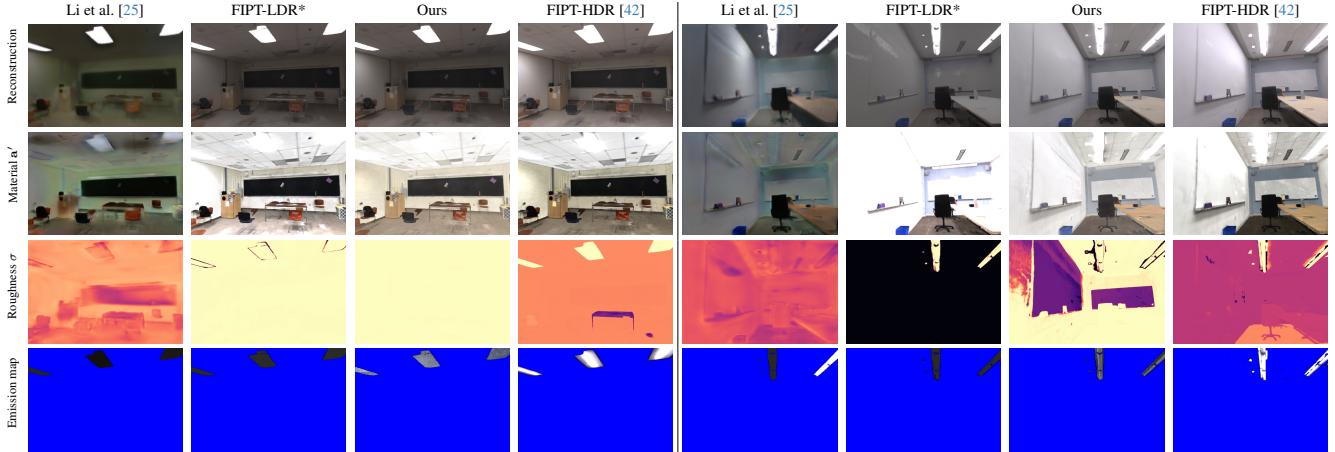


Figure 8. **Intrinsic decomposition of real scenes [42]**. From top to bottom, we show reconstruction, material reflectance  $\mathbf{a}'$ , roughness  $\sigma$ , and emission maps, following the same visualization in Figure 6.



Figure 9. **Novel view synthesis and relighting results on real scenes [42]**. The novel view synthesis results are shown on the left 4 columns, and the relighting of the same novel view are shown on the right 4 columns. FIPT-LDR\* bakes shading in the albedo and results in wrong roughness on the wall, which creates artifacts in novel illumination. In contrast, our method produce more clean and realistic shading.

Table 3. **Ablation of CRF modeling**. Mean CRF  $\bar{g}$ : mean curve  $\bar{g}$ , Gamma 1/2.2: exponential function  $g(x) = x^{1/2.2}$ .

Method	$k_d$	PSNR $\uparrow$		$L_2 \downarrow$
		$\mathbf{a}'$	$\sigma$	CRF
Constant exposure	24.24	19.11	<b>27.42</b>	4.074
Mean CRF $\bar{g}$	23.61	19.55	15.25	4.240
Gamma 1/2.2	23.65	20.05	15.72	3.683
Full model	<b>26.82</b>	<b>23.43</b>	26.63	<b>1.363</b>

even better specular/rough material separation than the FIPT-HDR method. Additionally, our proposed HDR emission estimation proves effective for real scenes, demonstrating the robust generalization capability of our framework.

#### 6.4. View Synthesis and Relighting on Real Scenes

We compare the novel view synthesis and relighting in Figure 9. We use the FIPT-HDR [42] as the reference for relighting in real scenes. The baseline methods perform well on the novel view synthesis task. However, ours produces better relighting quality and decomposition (see shading contrast on the floor and reflections on the whiteboard).

#### 6.5. Varying Exposure and CRF Modeling

We conduct an ablation study on various CRF choices, as detailed in Table 3. We parametrize the CRF as a continuous and monotonically increasing function across the domain  $(0, 1)$ . We uniformly sample 1024 points between 0 and 1 and calculate the L2 distance between the function values and the ground truth. Three CRF alternatives: constant exposure input, Mean CRF  $\bar{g}$  (the mean CRF from 201 empirical CRF functions measured in the real world [11]), and Gamma 1/2.2 ( $g(x) = x^{1/2.2}$ , as used in FIPT). Our method outperforms the single exposure approach, suggesting the benefits of using varying exposure values to enhance dynamic range. It also achieves better results than constant CRF functions, justifying joint CRF optimization’s merits.

#### 7. Limitations

Our emitter mask estimation may be inaccurate especially when images are largely saturated. An incorrect mask cannot be recovered from as masks are not further optimized. Our CRF model is global and it cannot capture complex non-local tone-mapping or while-balance changes. Addressing these issues would allow for a truly practical method for inverse rendering and is left for future work.

# IRIS: Inverse Rendering of Indoor Scenes from Low Dynamic Range Images

## Supplementary Material

### Abstract

This supplementary document shows additional details of our method and more results. We refer the readers to our supplementary webpage, which shows more results that allow for easy comparisons with the baseline methods on all scenes we use.

### 8. Implementation Details

To clarify the equations in the paper, we describe the mathematical expressions and associated physical meanings in [Table 4](#).

**Varying exposure data generation.** In real-world photography pipelines, exposure levels are adjusted by manipulating camera settings, such as shutter speed, aperture size, and ISO, to capture bright and dark regions. While the FIPT dataset [42] assumes single exposure and utilizes a simplistic camera response function (CRF) model defined as  $g(x) = x^{1/2.2}$ , our approach simulates a capturing process that is both more realistic and challenging. We split the HDR images of the same scene into five exposure levels  $\{t_i\}_{i=1}^5$ , s.t.  $t_i < t_{i+1}$ , where the brightest HDR image corresponds to  $t_0$ , and conversely, the darkest to  $t_5$ , effectively mimicking an auto-exposure mechanism. Subsequently, we apply each exposure level to the HDR image and convert it into LDR format with the CRF derived from real-world sensors [11].

**Direct illumination  $L_e(\mathbf{x})$ .** We first identify the mesh faces  $\{\mathbf{f}_i\}$  of emitters with the emitter mask  $M_e(\mathbf{x})$  defined on the mesh faces. We associate a learnable 3-dimensional parameter for each face:  $\mathbf{e}(\mathbf{f}) \in \mathbb{R}^3$ , representing the emitted light radiance. These parameters are then optimized during the HDR emission restoration phase.

**BRDF.** The surface material is represented as a neural field:  $(\mathbf{a}, m, \sigma) = \mathbf{F}(\mathbf{x})$ , the model architecture of which is based on Instant-NGP [31].

**Shading Baking.** Intuitively, the ray tracing continues if it encounters a non-emissive, specular surface (identified by a roughness threshold of 0.6), and stops otherwise. The radiance at the endpoint adheres to [Equation 9](#) in the main paper. The view-independent term  $L_{\text{SLF}}(\mathbf{x})$  effectively approximates the global illumination on diffuse surfaces, which also expedites the rendering process. This is because rays typically reach diffuse surfaces within a few bounces, eliminating the need for further path tracing.

Table 4. Notation table.

$(\cdot)_+$	dot product clamped to positive value
$\omega_i$	incident light direction
$\omega_o$	outgoing light direction
$\mathbf{h}$	half vector $(\omega_i + \omega_o)/\ \omega_i + \omega_o\ _2$
$\mathbf{n}$	surface normal
$\mathbf{x}$	3D position
$\mathbf{a}(\mathbf{x})$	surface albedo (base color)
$m(\mathbf{x})$	surface metallic
$\sigma(\mathbf{x})$	surface roughness
$\mathbf{k}_d(\mathbf{x})$	diffuse $\mathbf{a}(\mathbf{x})(1 - m(\mathbf{x}))$
$\mathbf{k}_s(\mathbf{x})$	specular $\mathbf{a}(\mathbf{x})m(\mathbf{x}) + 0.04(1 - m(\mathbf{x}))$
$D(\cdot)$	GGX normal distribution
$F(\cdot)$	Schlick’s approximation of Fresnel coefficients
$G(\cdot)$	Geometry (shadow-masking) term

Table 5. Ablation study.

Method	$k_d$	PSNR $\uparrow$		$L_2 \downarrow$
		$\mathbf{a}'$	$\sigma$	CRF
– Alternating opt.	22.206	19.331	18.238	1.995
– $\mathcal{L}_{\text{mat}}$	22.768	19.746	13.691	1.920
– $\mathcal{L}_{\text{CRF}}$	20.085	17.836	23.958	6.100
– $\mathcal{L}_{\text{albedo}}$	24.005	20.350	15.425	1.969
Full model	23.839	20.082	17.518	1.872

$$L_i(\mathbf{x}, \omega) = L_{\text{end}}(\mathbf{x}_n) \prod_{i=1}^{n-1} f(\mathbf{x}_{i+1} \rightarrow \mathbf{x}_i) \quad (14)$$

s.t.  $\sigma(\mathbf{x}_i) \leq 0.6, M_e(\mathbf{x}_i) = 0, \forall i < n,$

where  $\{\mathbf{x}_i\}_{i=1}^n$  are the intersected points along the paths.

### 9. Additional Ablation Study

We visualize the CRFs with different CRF modeling techniques in [Figure 10](#), corresponding to [Table 3](#) in the main paper. The results show that from input images captured with varying exposure, our method can recover ground truth CRF, demonstrating the effectiveness and importance of CRF modeling. Additionally, we depict the evolution of albedo at different stages of the process in [Figure 14](#), demonstrating the continuous improvement in the quality of albedo generated by our method throughout the optimization.

To validate the design choices of our method, we conducted an ablation study, the results of which are compared in terms of intrinsic decomposition quality in [Table 5](#). This

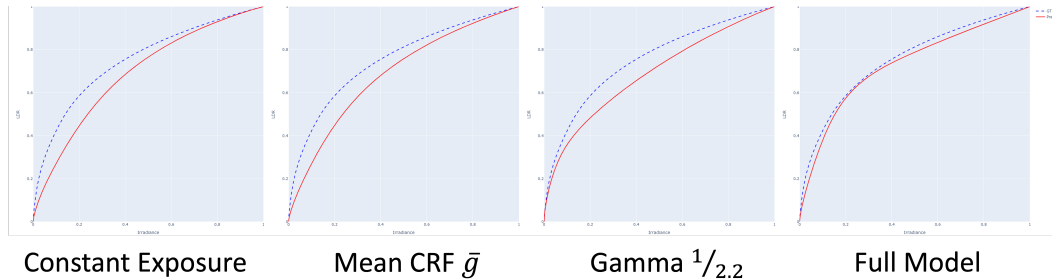


Figure 10. **CRF comparison visualization.** The blue dash lines are the ground-truth CRF and red lines are estimated CRF after the optimization. We show that full model with varying exposure and learnable CRF model is able to approximate the ground truth quite well.

evaluation was carried out on four synthetic scenes, with the report focusing on the average metric across these scenes. Without alternating optimization (‘– Alternating opt.’), the model suffers from inaccurate illumination estimation and shading baking, resulting in sub-optimal BRDF and CRF prediction. It is important to note that jointly optimizing BRDF, CRF, and emission presents a highly ill-posed and ambiguous challenge. Without the CRF regularization term  $\mathcal{L}_{\text{CRF}}$ , the CRF curve could appear highly unnatural. This aberration might not be evident in the photometric loss, as albedo and emission could be inaccurately adjusted to minimize this loss. Our method, with the inclusion of regularization terms, achieves the best CRF estimation when both  $\mathcal{L}_{\text{albedo}}$  and  $\mathcal{L}_{\text{mat}}$  are implemented.

## 10. Applications

Our method estimates accurate surface material and spatially varying illumination from LDR images, enabling various applications such as relighting and object insertion. We provide the qualitative results in Figure 11, Figure 12, and Figure 13. The results demonstrate effective modeling of specular reflections on smooth surfaces (like ‘tabletop’ and ‘whiteboard’) upon introducing new light sources. Moreover, our method accurately simulates inter-reflections between the scene and the inserted objects (such as a mirror ball and a diffuse ball), significantly elevating the realism of the object insertion. For more interactive visualizations and comparisons, please check our supplementary webpage.

## 11. Additional Evaluation Results

In addition to physically-based inverse rendering techniques like FIPT, methods based on neural radiance fields (NeRF) [30] strive for scene disentanglement by representing indoor scenes’ incident radiance fields with a 5D network [44] without constraints. Recent NeRF-based approaches like I<sup>2</sup>-SDF [52], NeILF++ [49], and NeFII [41], much like FIPT, rely on pre-calculated irradiance, and focus on surface rendering to reconstruct scene materials and/or lighting. However, these methods typically account for only single-bounce light



Figure 14. **Visualizing albedo during the training.** We show that leveraging data-driven Irisformer [53] estimation (Left) provides us good albedo initialization (Middle), and final result is refined with physically-based rendering model.

transport, leading to compromised quality in both material and lighting reconstruction. Here, we also include comparisons with NeILF [44] and I<sup>2</sup>-SDF [52] to highlight these distinctions.

The complete metrics of novel view synthesis and relighting are listed in Table 6. Our method achieves comparable novel view synthesis results and outperforms other baselines for relighting. The results underscore the effectiveness of our method in accurately decomposing intrinsic elements from LDR images.

Limitation-wise, the emitter estimation pipeline sometimes mistakenly identifies surfaces near strong emitters (like windows) as emitters themselves, leading to imprecise BRDF and illumination estimations. We have visualized these instances in Figure 15. The task of discerning emitters and light sources from LDR images remains a complex yet intriguing challenge, and we aim to address it in our future research.

## References

- [1] Dejan Azinovic, Tzu-Mao Li, Anton Kaplanyan, and Matthias Nießner. Inverse path tracing for joint material and lighting estimation. In *CVPR*, 2019. 2, 4
- [2] Sai Bi, Zexiang Xu, Pratul Srinivasan, Ben Mildenhall, Kalyan Sunkavalli, Miloš Hašan, Yannick Hold-Geoffroy, David Kriegman, and Ravi Ramamoorthi. Neural reflectance fields for appearance acquisition. *in arXiv*, 2020. 2
- [3] Bowen Cheng, Ishan Misra, Alexander G. Schwing,



Figure 11. **Relighting and object insertion in kitchen.** From top to bottom, we visualize the reconstruction (1st row), relighting (2nd row), and object insertion (3rd row).

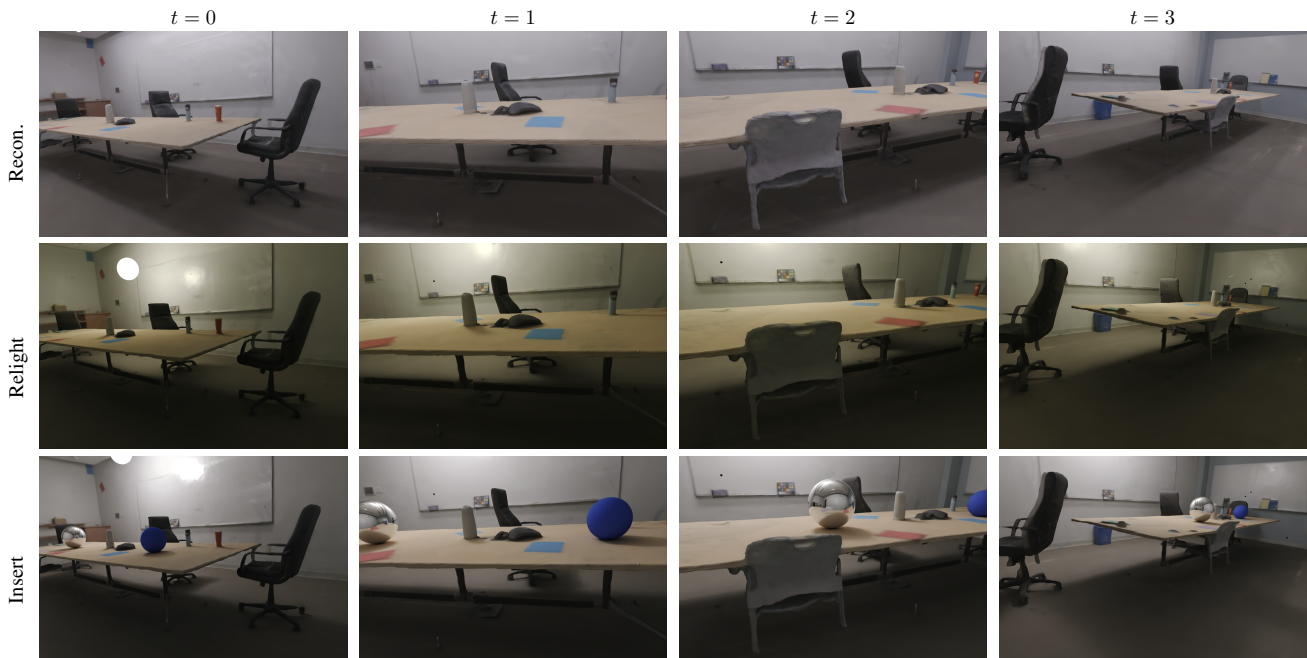


Figure 12. **Relighting and object insertion in 'conference room'.** From top to bottom, we visualize the reconstruction (1st row), relighting (2nd row), and object insertion (3rd row).

Alexander Kirillov, and Rohit Girdhar. Masked-attention mask transformer for universal image segmentation. In *CVPR*, 2022. 5

[4] Robert L Cook and Kenneth E. Torrance. A reflectance model for computer graphics. *ACM Transactions on Graphics (ToG)*, 1982. 3

[5] Mohammad Reza Karimi Dastjerdi, Jonathan Eisenmann, Yannick Hold-Geoffroy, and Jean-François

Lalonde. EverLight: Indoor-outdoor editable HDR lighting estimation. In *ICCV*, 2023. 3

[6] Paul E. Debevec and Jitendra Malik. Recovering high dynamic range radiance maps from photographs. In *SIGGRAPH*, 1997. 3

[7] Valentin Deschaintre, Miika Aittala, Fredo Durand, George Drettakis, and Adrien Bousseau. Single-image SVBRDF capture with a rendering-aware deep network.

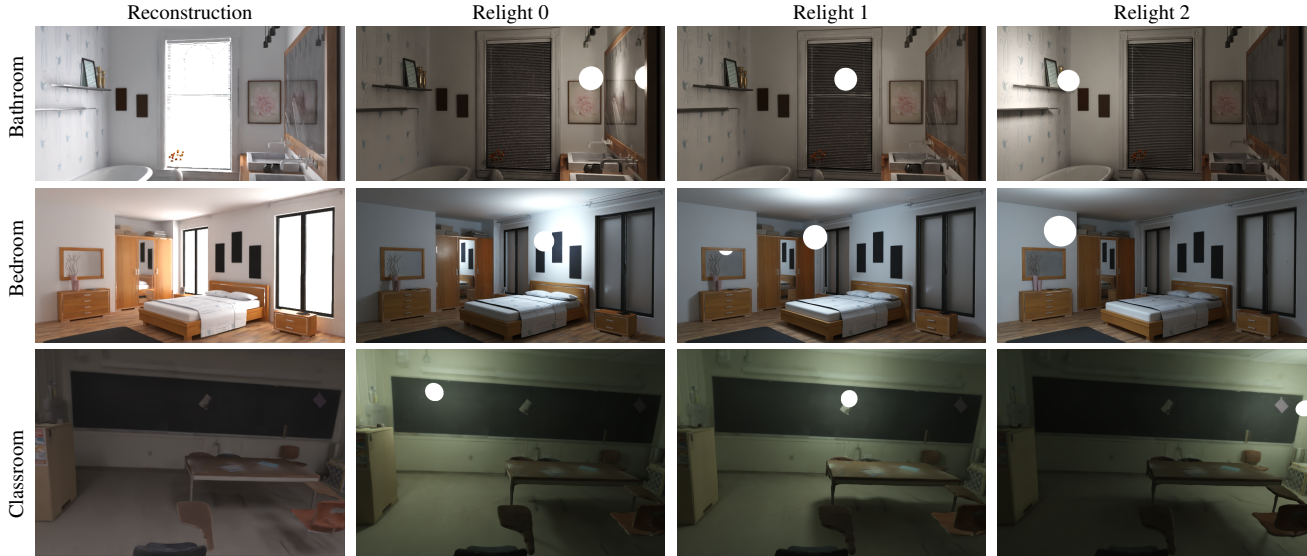


Figure 13. Relighting with moving light ball.

Table 6. Complete quantitative results of novel view synthesis and relighting on synthetic scenes

Method	Kitchen			Bedroom			Livingroom			Bathroom			
	PSNR $\uparrow$	SSIM $\uparrow$	LPIPS $\downarrow$	PSNR $\uparrow$	SSIM $\uparrow$	LPIPS $\downarrow$	PSNR $\uparrow$	SSIM $\uparrow$	LPIPS $\downarrow$	PSNR $\uparrow$	SSIM $\uparrow$	LPIPS $\downarrow$	
NVS	NeLF [44]	29.309	0.910	<b>0.187</b>	<b>29.651</b>	<b>0.944</b>	0.095	<b>34.653</b>	0.959	0.099	26.509	0.783	0.339
	I <sup>2</sup> -SDF [52]	24.993	0.898	0.234	25.845	0.916	0.150	27.955	<b>0.962</b>	<b>0.091</b>	24.967	0.698	0.483
	FIPT-LDR*	16.372	0.776	0.381	14.536	0.784	0.389	16.146	0.805	0.361	13.665	0.609	0.616
	Ours	<b>29.730</b>	<b>0.916</b>	0.192	28.765	0.940	<b>0.094</b>	31.368	0.954	0.104	<b>28.008</b>	<b>0.802</b>	<b>0.335</b>
	FIPT-HDR [42]	29.059	0.924	0.180	27.670	0.940	0.095	28.524	0.951	0.109	29.788	0.792	0.358
Relight	Li22 [25]	21.755	0.815	0.381	23.662	0.851	0.342	<b>21.631</b>	0.841	0.395	22.887	0.747	0.475
	FIPT-LDR*	11.932	0.715	0.283	13.132	0.701	0.334	9.198	0.710	0.345	12.240	0.694	0.473
	Ours	<b>23.818</b>	<b>0.873</b>	<b>0.143</b>	<b>25.483</b>	<b>0.892</b>	<b>0.166</b>	18.478	<b>0.906</b>	<b>0.127</b>	<b>23.664</b>	<b>0.856</b>	<b>0.254</b>
	FIPT-HDR [42]	27.597	0.886	0.115	28.411	0.878	0.155	32.543	0.964	0.078	27.497	0.881	0.208

*ACM Transactions on Graphics (ToG)*, 37(4):128:1–15, 2018. 2

- [8] Marc-André Gardner, Kalyan Sunkavalli, Ersin Yumer, Xiaohui Shen, Emiliano Gambaretto, Christian Gagné, and Jean-François Lalonde. Learning to predict indoor illumination from a single image. *ACM Transactions on Graphics*, 36(6):176:1–14, 2017. 2
- [9] Marc-André Gardner, Yannick Hold-Geoffroy, Kalyan Sunkavalli, Christian Gagné, and Jean-François Lalonde. Deep parametric indoor lighting estimation. In *ICCV*, 2019. 3
- [10] Dan B Goldman, Brian Curless, Aaron Hertzmann, and Steven M Seitz. Shape and spatially-varying brdfs from photometric stereo. *IEEE Transactions on Pattern Analysis and Machine Intelligence*, 32(6):1060–1071, 2009. 2
- [11] Michael D. Grossberg and Shree K. Nayar. Modeling the space of camera response functions. *IEEE TPAMI*, 26(10):1272–1282, 2004. 3, 4, 8, 9
- [12] Yannick Hold-Geoffroy, Kalyan Sunkavalli, Sunil Hadap, Emiliano Gambaretto, and Jean-François Lalonde. Deep outdoor illumination estimation. In *CVPR*, 2017. 3
- [13] Yannick Hold-Geoffroy, Akshaya Athawale, and Jean-François Lalonde. Deep sky modeling for single image outdoor lighting estimation. In *CVPR*, 2019. 3
- [14] Wenzel Jakob, Sébastien Speierer, Nicolas Roussel, Merlin Nimier-David, Delio Vicini, Tizian Zeltner, Baptiste Nicolet, Miguel Crespo, Vincent Leroy, and Ziyi Zhang. Mitsuba 3 renderer, 2022. <https://mitsuba-renderer.org>. 2
- [15] Haiyan Jin, Isabella Liu, Peijia Xu, Xiaoshuai Zhang, Songfang Han, Sai Bi, Xiaowei Zhou, Zexiang Xu, and Hao Su. TensorIR: Tensorial inverse rendering. In *CVPR*, 2023. 4
- [16] James T Kajiya. The rendering equation. In *SIG-*

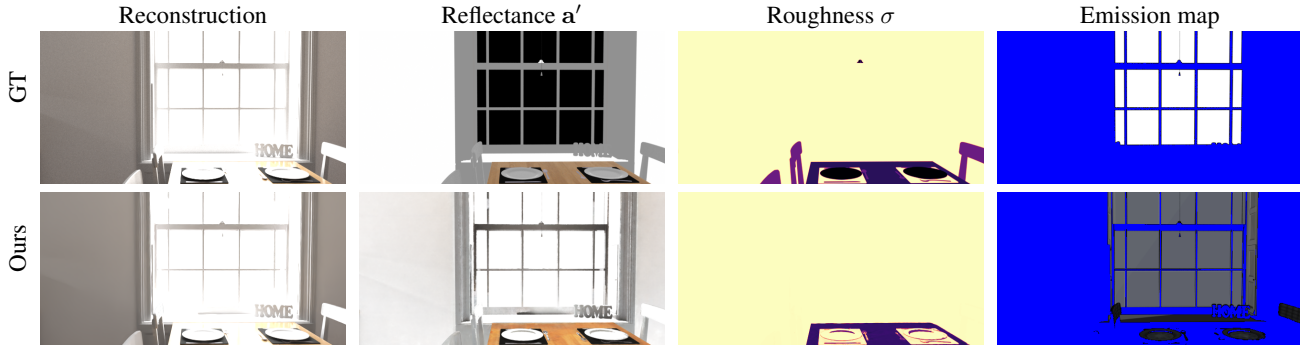


Figure 15. Failure cases.

- GRAPH, 1986. 3
- [17] Jaroslav Krivánek and Pascal Gautron. *Practical global illumination with irradiance caching*. Springer, 2022. 3
- [18] Eric Lafortune. *Mathematical models and Monte Carlo algorithms for physically based rendering*. PhD thesis, Katholieke Universiteit Leuven, 1996. 3
- [19] Xiao Li, Yue Dong, Pieter Peers, and Xin Tong. Modeling surface appearance from a single photograph using self-augmented convolutional neural networks. *ACM Transactions on Graphics (ToG)*, 36(4):45:1–11, 2017. 2
- [20] Zhengqi Li and Noah Snavely. CGIntrinsics: Better intrinsic image decomposition through physically-based rendering. In *ECCV*, 2018. 2
- [21] Zhengqi Li and Noah Snavely. Learning intrinsic image decomposition from watching the world. In *CVPR*, 2018. 2
- [22] Zhengqin Li, Kalyan Sunkavalli, and Manmohan Chandraker. Materials for masses: SVBRDF acquisition with a single mobile phone image. In *ECCV*, 2018. 2
- [23] Zhengqin Li, Mohammad Shafiei, Ravi Ramamoorthi, Kalyan Sunkavalli, and Manmohan Chandraker. Inverse rendering for complex indoor scenes: Shape, spatially-varying lighting and svbrdf from a single image. In *CVPR*, 2020. 2
- [24] Zhengqin Li, Ting-Wei Yu, Shen Sang, Sarah Wang, Meng Song, Yuhan Liu, Yu-Ying Yeh, Rui Zhu, Nitesh Gundavarapu, Jia Shi, et al. OpenRooms: An open framework for photorealistic indoor scene datasets. In *CVPR*, 2021. 2
- [25] Zhengqin Li, Jia Shi, Sai Bi, Rui Zhu, Kalyan Sunkavalli, Miloš Hašan, Zexiang Xu, Ravi Ramamoorthi, and Manmohan Chandraker. Physically-based editing of indoor scene lighting from a single image. In *ECCV*, 2022. 2, 6, 7, 8, 12
- [26] Zhaoshuo Li, Thomas Müller, Alex Evans, Russell H. Taylor, M. Unberath, Ming-Yu Liu, and Chen-Hsuan Lin. Neuralangelo: High-fidelity neural surface reconstruction. In *CVPR*, 2023. 4
- [27] Yu-Lun Liu, Wei-Sheng Lai, Yu-Sheng Chen, Yi-Lung Kao, Ming-Hsuan Yang, Yung-Yu Chuang, and Jia-Bin Huang. Single-image HDR reconstruction by learning to reverse the camera pipeline. In *CVPR*, 2020. 3, 4
- [28] William E Lorensen and Harvey E Cline. Marching cubes: A high resolution 3D surface construction algorithm. *Computer Graphics*, 1987. 6
- [29] Demetris Marnerides, Thomas Bashford-Rogers, Jonathan Hatchett, and Kurt Debattista. Expandnet: A deep convolutional neural network for high dynamic range expansion from low dynamic range content. *Computer Graphics Forum*, 2018. 3
- [30] Ben Mildenhall, Pratul P. Srinivasan, Matthew Tancik, Jonathan T. Barron, Ravi Ramamoorthi, and Ren Ng. Nerf: Representing scenes as neural radiance fields for view synthesis. In *ECCV*, 2020. 6, 10
- [31] Thomas Müller, Alex Evans, Christoph Schied, and Alexander Keller. Instant neural graphics primitives with a multiresolution hash encoding. *ACM TOG*, 2022. 9
- [32] Merlin Nimier-David, Zhao Dong, Wenzel Jakob, and Anton Kaplanyan. Material and lighting reconstruction for complex indoor scenes with texture-space differentiable rendering. In *Eurographics Symposium on Rendering*, 2021. 2, 4
- [33] Julien Philip, Sébastien Morgenthaler, Michaël Gharbi, and George Drettakis. Free-viewpoint indoor neural relighting from multi-view stereo. *ACM Trans. Graph.*, 40(5):194:1–18, 2021. 2
- [34] Erik Reinhard, Greg Ward, Sumanta Pattanaik, Paul Debevec, Wolfgang Heidrich, and Karol Myszkowski. *High Dynamic Range Imaging – Acquisition, Display and Image-Based Lighting*. Morgan Kaufmann, 2nd edition, 2010. 1
- [35] Mike Roberts, Jason Ramapuram, Anurag Ranjan, Atulit Kumar, Miguel Angel Bautista, Nathan Paczan,

- Russ Webb, and Joshua M. Susskind. Hypersim: A photorealistic synthetic dataset for holistic indoor scene understanding. In *ICCV*, 2021. 2
- [36] Dario Seyb, Peter-Pike Sloan, Ari Silvennoinen, Michał Iwanicki, and Wojciech Jarosz. The design and evolution of the uberbake light baking system. *ACM Transactions on Graphics (TOG)*, 2020. 3
- [37] Pratul P Srinivasan, Ben Mildenhall, Matthew Tancik, Jonathan T Barron, Richard Tucker, and Noah Snavely. Lighthouse: Predicting lighting volumes for spatially-coherent illumination. In *CVPR*, 2020. 2
- [38] Pratul P. Srinivasan, Boyang Deng, Xiuming Zhang, Matthew Tancik, Ben Mildenhall, and Jonathan T. Barron. NeRV: Neural reflectance and visibility fields for relighting and view synthesis. In *CVPR*, 2021. 2, 4
- [39] Zian Wang, Jonah Philion, Sanja Fidler, and Jan Kautz. Learning indoor inverse rendering with 3D spatially-varying lighting. In *ICCV*, 2021. 2, 3
- [40] Zian Wang, Tianchang Shen, Jun Gao, Shengyu Huang, Jacob Munkberg, Jon Hasselgren, Zan Gojcic, Wenzheng Chen, and Sanja Fidler. Neural fields meet explicit geometric representations for inverse rendering of urban scenes. In *CVPR*, 2023. 2, 3, 4
- [41] Haoqian Wu, Zhipeng Hu, Lincheng Li, Yongqiang Zhang, Changjie Fan, and Xin Yu. NeFII: Inverse rendering for reflectance decomposition with near-field indirect illumination. In *CVPR*, 2023. 2, 10
- [42] Liwen Wu, Rui Zhu, Mustafa B Yaldiz, Yinhao Zhu, Hong Cai, Janarбек Matai, Fatih Porikli, Tzu-Mao Li, Manmohan Chandraker, and Ravi Ramamoorthi. Factorized inverse path tracing for efficient and accurate material-lighting estimation. In *ICCV*, 2023. 2, 4, 5, 6, 7, 8, 9, 12
- [43] Xin Yang, Ke Xu, Yibing Song, Qiang Zhang, Xiaopeng Wei, and Rynson WH Lau. Image correction via deep reciprocating HDR transformation. In *CVPR*, 2018. 3
- [44] Yao Yao, Jingyang Zhang, Jingbo Liu, Yihang Qu, Tian Fang, David McKinnon, Yanghai Tsin, and Long Quan. NeILF: Neural incident light field for physically-based material estimation. In *ECCV*, 2022. 6, 7, 8, 10, 12
- [45] Bohan Yu, Siqi Yang, Xuanning Cui, Siyan Dong, Baoquan Chen, and Boxin Shi. MILO: Multi-bounce inverse rendering for indoor scene with light-emitting objects. *IEEE TPAMI*, 2023. 2, 4
- [46] Zehao Yu, Songyou Peng, Michael Niemeyer, Torsten Sattler, and Andreas Geiger. MonoSDF: Exploring monocular geometric cues for neural implicit surface reconstruction. In *NeurIPS*, 2022. 4, 5, 6
- [47] Jinsong Zhang and Jean-François Lalonde. Learning high dynamic range from outdoor panoramas. In *ICCV*, 2017. 3
- [48] Jinsong Zhang, Kalyan Sunkavalli, Yannick Hold-Geoffroy, Sunil Hadap, Jonathan Eisenman, and Jean-François Lalonde. All-weather deep outdoor lighting estimation. In *CVPR*, 2019. 3
- [49] Jingyang Zhang, Yao Yao, Shiwei Li, Jingbo Liu, Tian Fang, David McKinnon, Yanghai Tsin, and Long Quan. NeILF++: Inter-reflectable light fields for geometry and material estimation. In *ICCV*, 2023. 2, 10
- [50] Kai Zhang, Fujun Luan, Qianqian Wang, Kavita Bala, and Noah Snavely. PhysSG: Inverse rendering with spherical gaussians for physics-based material editing and relighting. In *CVPR*, 2021. 4
- [51] Xiuming Zhang, Pratul P. Srinivasan, Boyang Deng, Paul Debevec, William T. Freeman, and Jonathan T. Barron. NeRFactor: Neural factorization of shape and reflectance under an unknown illumination. *ACM Trans. Graph.*, 40(6):237:1–18, 2021. 2
- [52] Jingsen Zhu, Yuchi Huo, Qi Ye, Fujun Luan, Jifan Li, Dianbing Xi, Lisha Wang, Rui Tang, Wei Hua, Hujun Bao, and Rui Wang. I<sup>2</sup>-SDF: Intrinsic indoor scene reconstruction and editing via raytracing in neural SDFs. In *CVPR*, 2023. 2, 4, 10, 12
- [53] Rui Zhu, Zhengqin Li, Janarбек Matai, Fatih Porikli, and Manmohan Chandraker. IRISformer: Dense vision transformers for single-image inverse rendering in indoor scenes. In *CVPR*, 2022. 2, 4, 10